

Research article

## Optimization of leg mechanism and design of a PD control for a quadruped robot

Mobin Salehi<sup>1\*</sup>, Arash Emami<sup>2</sup> and Mojtaba Norozi<sup>3</sup>

<sup>1</sup>Mechanical Engineering Department, Sharif University of Technology, Tehran, Tehran, Iran

<sup>2</sup>Mechanical Engineering Department, Islamic Azad University of Central Tehran Branch, Tehran, Tehran, Iran

<sup>3</sup>Industrial Engineering Department, Malek Ashtar University of Technology, Tehran, Tehran, Iran

\*Mobin.Salehi93@gmail.com

(Manuscript Received --- 14 Oct. 2024; Revised --- 25 Dec. 2024; Accepted --- 30 Dec. 2024)

---

### Abstract

This paper presents the design and control of a quadruped robot. One of the primary challenges in building quadruped robots is the need for high torque density actuators and an efficient control algorithm. To address these challenges, this work focuses on optimizing the transmission torque ratio of the 4-bar linkage used in the robot's legs, using a genetic algorithm. The optimization is achieved by deriving the kinematic equations of the robot's legs and introducing a novel objective function tailored to the robot's application. To evaluate the impact of the optimization, the full dynamics of the robot are derived and validated through variations in total mechanical energy. A kinematics-based controller, suitable for real-time applications, is proposed, and its performance is tested in various scenarios to assess its effectiveness. The controller is applied to robots with two different linkage lengths, one optimized for maximum and the other for minimum torque requirements. The results show that the optimization reduces the required torque by nearly 42% when comparing the maximum to the minimum case.

*Keywords:* Quadruped robots, Genetic algorithm, Model-independent controller, Four-bar linkage, Mechanism optimization.

---

### 1- Introduction

Legged robots, with their unique abilities, can traverse uneven terrain more easily compared to wheeled robots. Due to the configuration of these robots, their locomotion can adapt to the environment [1, 2], allowing them to handle tasks in unknown or unpredictable conditions. Researchers have also explored combining wheeled and quadruped robots to leverage the advantages of both systems [3].

Among legged robots, quadrupeds are a major area of research because their design

offers greater stability compared to bipedal robots. The design of quadruped robots is often inspired by nature, with researchers trying to mimic the locomotion of animals like dogs [4], cats [5], turtles [6], and cheetahs [7]. These robots can be deployed in environments that reduce the risk of human injury while improving overall performance. Some of their applications include inspection, search and rescue, delivery, monitoring, and more.

Quadruped robots can be classified into different categories based on their actuators,

topology, configuration, and more [8]. Depending on the robot's application, the type of actuators may vary. The most common actuators used in such robots are electrical, pneumatic, and hydraulic. Hydraulic actuators are typically used for tasks that involve carrying heavy loads. Robots like BigDog, LS3, and WildCat are examples of those utilizing hydraulic actuators [9, 10, 11]. Electrical actuators, which are gaining popularity in recent research, have been increasingly adopted. For instance, MIT's new electrical actuator design for impedance control in quadruped robots has led many researchers to switch to electrical actuators. Mini Cheetah is a well-known example of a lightweight quadruped robot using these actuators [12,13]. Another prominent robot is ANYmal from ETH Zurich, which is recognized for its ability to operate in unknown environments and is often used for industrial inspection. Lastly, pneumatic actuators are less commonly used due to their lower control accuracy. However, some researchers favor them for their lightweight properties [14].

One of the critical components of a quadruped robot that has a tremendous influence on the robot's locomotion stability and adaptability is robots' legs [15]. There are various types of leg designs that can categorize quadruped robots into different groups. Some examples include rigid legs, articulated legs, parallel mechanisms, and spring-loaded legs, among others [16-18]. Some researchers are exploring flexible materials to enhance robot degrees of freedom and ensure safer interaction. One innovative approach involves using honeycomb-structured flexible materials for robot legs, combined with pneumatic actuators. This design effectively reduces the robot's total weight while maintaining functional integrity [19]. Additionally, leg

structures incorporating tensegrity mechanisms have been explored in research [20]. The study primarily focused on enhancing the payload capacity of the tensegrity mechanism to make it viable for use in quadruped robots.

Quadruped robots can also generate different gaits through various combinations of leg movements, which contribute to both stability and locomotion speed. Common gaits include walking, trotting, pacing, and more [21]. Recently a study investigated the relationship between different gaits and stability by employing mathematical models rooted in spiral theory [22]. Similarly, the main body of the robot (torso) can be divided into two categories: rigid and flexible [23, 24]. In flexible torsos, the robot can achieve higher speeds, but designing an efficient control algorithm for such torsos is more challenging compared to rigid ones.

Prior to motion control, path planning has been a critical area of investigation in robotics research. For instance, two staged optimization approach was explored in a study to enhance the robot's performance in densely clustered environments [25]. The control algorithms for quadruped robots can be divided into model-independent and model-based methods. Generally speaking, each leg of the robot has three degrees of freedom: two for pitching and one for rolling [26]. Some model-independent methods use concepts like Central Pattern Generators (CPGs) to generate periodic motions [27, 28]. These types of oscillators require fewer feedback inputs compared to model-based controllers. For more robust control, researchers use model-based controllers. Due to the complex dynamics of the system, a simplified kinematic model that approximates the robot's behavior is often employed in the control algorithm.

The spring-loaded inverted pendulum (SLIP) model is commonly used as it approximates the behavior of such systems well [29]. This simplified model can be applied in methods like Model Predictive Control (MPC) to design control signals based on the predicted future response of the system [30, 31]. In contrast, some approaches rely on more accurate dynamic modeling, such as Whole Body Dynamics [26]. Also, a virtual method has been presented that models the ground reaction as a virtual spring. The task of the controller is to control the reaction virtual forces via actuators through the Jacobian matrix [33]. An accurate design plays a significant role in the stability, agility, and performance of quadruped robots [26], and therefore must be carefully considered. In this article, we focus on the design of quadruped robots equipped with electrical actuators and a four-bar linkage mechanism. To achieve optimal performance in force transmission, a heuristic optimization approach has been applied to the link lengths. Subsequently, the kinematic and kinetic equations of the robot have been derived to design a PD controller based on the dynamic model. Finally, the results of the controller, both with and without optimization, have been compared to evaluate the effectiveness of the design. This article employs a genetic algorithm to optimize the lengths of a quadruped robot's links based on a proposed cost function and constraints. The optimization reduces the required torque for forward motion, enabling the use of lightweight actuators in the robot's main torso, improving performance and reducing costs. Additionally, a model-independent controller is presented for real-time applications. The article systematically derives and explains the robot's kinematics

and dynamics, emphasizing efficiency in design and control.

In the first section, the 4-bar linkages of the robot's leg are optimized through the kinematic equations and transmission ratio. In the next section, the entire kinematics of the leg is expressed, and the robot's desired path, considering the kinematic equations, is developed using polynomial equations. Subsequently, the dynamics of the robot are modeled and verified. After this section, the control algorithm is presented based on two phases of the robot's dynamics. The results section demonstrates the control performance of the proposed algorithm and compares the results of the length optimization. Finally, the findings are summarized, and future work is suggested.

## 2- Four bar linkage

The robot's conceptual design of robot is illustrated in Fig. 1. Each leg of the robot consists of two joints for pitching (the hip and knee joints) and one joint for rolling (the thigh joint), resulting in three degrees of freedom (DOF) to control the robot's movement. To reduce the inertia of the robot's leg, no actuators are placed directly on the leg itself. Instead, all motors are located on the torso of the robot, necessitating a transmission mechanism for the knee joints. Two common methods for transmitting knee torque are timing belts and four-bar linkages [34, 35]. The concept of the robot's leg for pitching is depicted in Fig. 2.



Fig. 1 The conceptual design of quadruped robot.

The four-bar linkage shown in Fig. 2 functions like a gear with a unique gear ratio. Consequently, the lengths of the four-bar links are optimized to achieve maximum torque at the output.

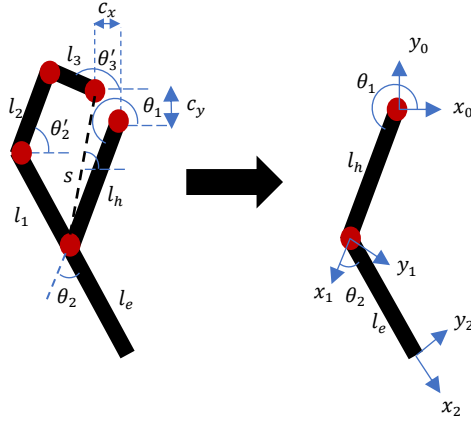


**Fig. 2** Robot's leg considering 4 bar mechanism and showing the simplified version as a 2 link.

The dynamics of the robot's leg is divided into two parts. In the swing phase, the actuators function to step forward without any contact with the ground. In contrast, during the stance phase, the robot remains in contact with the ground. The main objective of the optimization is to reduce the torque density of the actuators. This can be achieved by selecting appropriate link lengths to enhance force transmission efficiency. Therefore, the four-bar linkage mechanism needs to be analyzed.

Figure 3 illustrates the four-bar linkage used in the robot's leg.

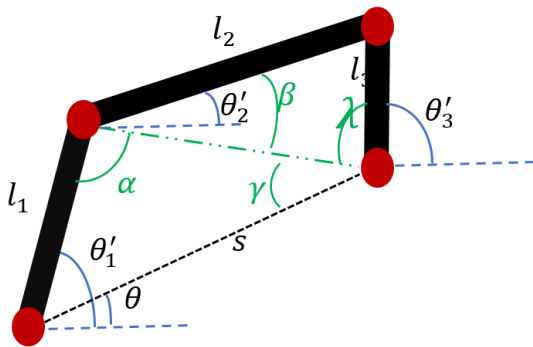


**Fig. 3** The 4-bar mechanism of leg.

Since the four-bar linkage is a one-degree-of-freedom (DOF) system, only the angle  $\theta'_1$  is considered as the input angle generated from the desired angle in the robot's leg, which is given by  $\theta_1 + \theta_2 - \pi$ . Based on the angles of the other links can be expressed as follows:

$$\theta'_2 = \beta - \gamma + \theta \quad (1)$$

$$\theta'_3 = \pi - (\lambda + \gamma - \theta) \quad (2)$$

In Eqs. (1) and (2), the  $\lambda$  and  $\gamma$  equals to:

$$\gamma = \sin^{-1}\left(\frac{l_1}{l_3} \sin(\theta'_1 - \theta)\right) \quad (3)$$

$$\lambda = \sin^{-1}\left(\frac{l_2}{l_3} \sin \beta\right) \quad (4)$$

which  $\beta$  is calculated as below:

$$\beta = \cos^{-1}\left(\frac{l_2^2 + l_1^2 + s^2 - 2l_1s \cos(\theta'_1 - \theta) - l_3^2}{2l_2\sqrt{l_1^2 + s^2 - 2l_1s \cos(\theta'_1 - \theta)}}\right) \quad (5)$$

In a conventional four-bar mechanism, the angle  $\theta$  and the distance  $s$  between the first and last joint (as shown in Fig. 3) are fixed. However, due to the rotation of the robot's actuator, these values can change, as illustrated in Fig. 2.

The angle  $\theta$  is given by:

$$\theta = \tan^{-1}\left(\frac{c_y - l_h \sin \theta_1}{c_x - l_h \cos \theta_1}\right) \quad (6)$$

which  $c_x$  and  $c_y$  are the distance between robot's actuators according to Fig. 2. The distance  $s$  is calculated as:

$$s = \sqrt{(c_y - l_h \sin \theta_1)^2 + (c_x - l_h \cos \theta_1)^2} \quad (7)$$

As all of the angles in the four-bar linkage are defined, the transmission angle, which relates the output to the input torque, can be formulated. The force diagram of the four-bar linkage is shown in Fig. 4.

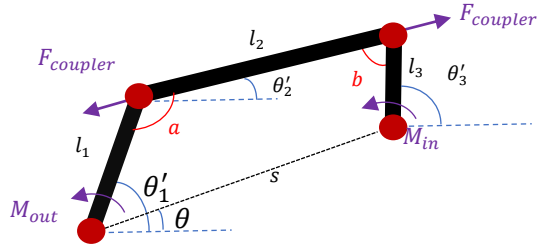


**Fig. 4** The force diagram of four bar linkage.

As shown in Fig. 4, the output torque to the input torque is given by:

$$\frac{M_{out}}{M_{in}} = \frac{l_1 \sin a}{l_3 \sin b} \quad (8)$$

The angles between the linkages are denoted by  $a$  and  $b$ , as depicted in Fig. 4. Since the robot's leg has low inertia during the stance phase, we can consider it a stationary phase, making Eq. (8) criteria applicable in this context.

The main objective of the optimization is to determine the lengths that maximize the transmission ratio. This can be achieved by selecting appropriate lengths. To find the optimal lengths, a genetic algorithm is employed, as it is well-suited for handling the numerous constraints present in the mechanism through principles of natural selection. The chosen cost function is defined as follows:

$$\begin{aligned} cost &= \sum_{\theta_2} \sum_{\theta_1} \left| \frac{l_1 \sin a}{l_3 \sin b} \right| \\ &+ \sum_{\theta_2} \sum_{\theta_1} f(\theta_1, \theta_2, l_1, l_2, l_3) \end{aligned} \quad (9)$$

The first part of Eq. (9) calculates the absolute value of the transmission ratio for different input angles, while the second part checks the feasibility of these angles and lengths within the four-bar mechanism. This is defined as follows:

$$f(\theta_1, \theta_2, l_1, l_2, l_3) = \begin{cases} 5, & g == 0 \\ -50, & otherwise \end{cases} \quad (10)$$

which function  $g$  is derived from Freudenstein's Equation [36] and is expressed as follows:

$$\begin{aligned} g &= \cos(\theta'_1 - \theta'_3) - \frac{l_1^2 + l_3^2 + s^2 - l_2^2}{2l_1 l_3} \\ &+ \frac{s}{l_3} \cos(\theta'_1 - \theta) \\ &- \frac{s}{l_1} \cos(\theta'_3 - \theta) \end{aligned} \quad (11)$$

In Eq. (10), if the configuration is valid, the combination yields a positive value that contributes to increasing the cost. Conversely, if the possibility condition is violated, the response is penalized with a negative cost.

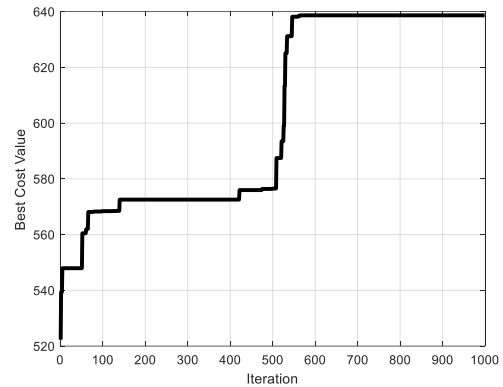


**Fig. 5** The cost function of optimizing lengths over the iteration.

To maximize the cost function, the offspring population (60 percent of the parent population) is generated through single, double, and uniform crossovers. Additionally, the mutant population (90 percent of the total population) is created by applying a normal probability function to the parents. The roulette wheel selection method is employed for choosing parents, and the termination condition is based on reaching the maximum number of iterations. Also, there are 150 chromosomes in the population, and each chromosome

contains 3 genes, which represent the lengths of the four-bar mechanism. Before conducting the optimization, the intervals for angles  $\theta_1$  and  $\theta_2$  were selected to ensure that the robot could operate within a desired workspace for a specific geometry, as it is not designed to reach arbitrary angles. The range for  $\theta_1$  was discretized into 10 steps spanning from  $-110$  deg to  $-140$ deg, while  $\theta_2$  was defined across 10 steps ranging from  $20$ deg to  $70$ deg. There is one extreme case that can lead to a high value of the transmission ratio, which occurs when links 2 and 3 are aligned. The genetic algorithm tends to reach this configuration in each run; however, due to the singularity associated with this alignment, it is considered a violation and is thus avoided. The resulting lengths of the links are  $l_1 = 0.1822$  m,  $l_2 = 0.1977$  m and  $l_3 = 0.1822$  m respectively. Fig. 5 illustrates the convergence plot over the iterations.

To compare these results with other values, the minimum of the cost function is derived by inverting the first part of the formula. Table 1 presents three cases of the robot's leg, two of which are generated from the genetic algorithm, while one represents a feasible solution for the robot's configuration.

**Table 1:** The results of GA optimization on robot's links.

Response	$l_1$ (cm)	$l_2$ (cm)	$l_3$ (cm)	$l_h$ (cm)	$l_e$ (cm)
Ordinary response	6	15	6	15	15
Maximum ratio	18.22	19.77	18.22	15	15
Minimum Ratio	12.88	8.83	12.88	15	15

In the next section, the kinematic model of the robot's leg is developed, and the desired trajectory for the robot's leg is presented.

### 3- Kinematic analysis

In the previous section, the kinematic equations of the four-bar linkage were developed. To determine the desired angles of the links, the inverse and forward kinematics of the two-bar linkage (as shown on the right side of Fig. 2) must be formulated. The Denavit-Hartenberg (DH) parameters for the series section are shown in Table 2.

**Table 2:** The DH parameters of series links.  $i$  denotes link's number.

$d_i$	$\theta_i$	$a_i$	$\alpha_i$
0	$\theta_1$	$l_h$	0
0	$\theta_2$	$l_e$	0

The position of the leg's end effector for rolling in the  $x_0y_0z_0$  coordinate system is given below:

$$P_{contact} = \begin{Bmatrix} l_h \cos \theta_1 + l_e \cos(\theta_1 + \theta_2) \\ l_h \sin \theta_1 + l_e \sin(\theta_1 + \theta_2) \\ 0 \end{Bmatrix} \quad (12)$$

The velocity of end effector, according to Eq. (12) is given by:

$$\begin{Bmatrix} \dot{p}_x \\ \dot{p}_y \end{Bmatrix} = [A] \begin{Bmatrix} \dot{\theta}_1 \\ \dot{\theta}_2 \end{Bmatrix} \quad (13)$$

which matrix  $A$  can be represented by:

$$[A] = \begin{bmatrix} -l_h \sin \theta_1 - l_e \sin(\theta_1 + \theta_2) & -l_e \sin(\theta_1 + \theta_2) \\ l_h \cos \theta_1 + l_e \cos(\theta_1 + \theta_2) & l_e \cos(\theta_1 + \theta_2) \end{bmatrix} \quad (14)$$

By inverting Eq. (14), the joint angular velocities of the robot can be calculated for a given desired trajectory.

$$\begin{Bmatrix} \dot{\theta}_1 \\ \dot{\theta}_2 \end{Bmatrix} = [A]^{-1} \begin{Bmatrix} \dot{p}_x \\ \dot{p}_y \end{Bmatrix} \quad (15)$$

The desired angles of the two links can be obtained by integrating the desired angular velocities in Eq. (15).

Now, the desired trajectory of the robot's leg can be developed. Generally, the robot's movement consists of two phases. Here, the desired trajectory for the swing phase is developed. Polynomial functions are used to define the desired trajectory based on the problem's conditions [37]. While other methods, such as trigonometric and Bezier functions, can also represent the desired trajectory, polynomial functions are chosen because they meet the specific requirements for velocity and position constraints.

In order to reduce the order of the polynomials, the swing phase trajectory is divided into two parts: the acceleration phase and the deceleration phase [37]. The conditions for these two phases follow the same concept, which requires that the initial and final positions, velocities, and accelerations must be continuous. As an example, the conditions for the x-direction in the acceleration phase can be written as follows [37]:

$$\begin{aligned}
 x_{SW,0} &= -L/2 \\
 \frac{dx_{SW,0}}{dt} &= \frac{dx_{ST,f}}{dt} \\
 \frac{d^2x_{SW,0}}{dt^2} &= \frac{d^2x_{ST,f}}{dt^2} \\
 x_{SW,0.5T_{SW}} &= 0 \\
 \frac{dx_{SW,0.5T_{SW}}}{dt} &= \alpha \frac{dx_{ST,f}}{dt} \\
 \frac{d^2x_{SW,0.5T_{SW}}}{dt^2} &= 0
 \end{aligned} \tag{16}$$

The subscripts *SW* and *ST* refer to the swing and stance phases, respectively. The value following the motion phase indicates the time, where 0 represents the initial time of the phase, and *f* represents the final time. The parameter  $\alpha$  represents the acceleration during the acceleration phase and *L* declares

the step length. Given the six specified conditions (continuity of position, velocity, and acceleration), the polynomial has an order of 5. During the robot's stance phase, the controller's primary task is to propel the robot forward. Following the stance phase, the robot transitions into the swing phase. Utilizing (16) conditions as an example for the acceleration path of the leg endpoint in the x-direction (the deceleration phase and y-direction can be similarly derived), the robot's virtual path in the stance phase defines the desired swing phase trajectory. By fixing the torso and assuming inverse leg movement, terms such as  $\frac{dx_{ST,f}}{dt}$ ,  $\frac{d^2x_{ST,f}}{dt^2}$  can be computed.

The desired polynomials, based on the leg's conditions, can be expressed as follows:

$$x_{SW}(t) = b_5t^5 + b_4t^4 + b_3t^3 + b_2t^2 + b_1t + b_0 \tag{17}$$

$$y_{SW}(t) = a_5t^5 + a_4t^4 + a_3t^3 + a_2t^2 + a_1t + a_0 \tag{18}$$

Based on the mentioned conditions, the constant terms in Eqs. (17) and (18) can be computed. These constants depend on the virtual path of the stance phase, which is determined through the control algorithm in real-time operation. In Fig. 6, the desired trajectory is depicted for a maximum height of 8 cm, an initial position (*L*/2) of 10 cm in the x-direction, and a swing time of 0.7 seconds. This trajectory ensures smooth transitions during the swing phase while adhering to the specified conditions in Eq. (16).

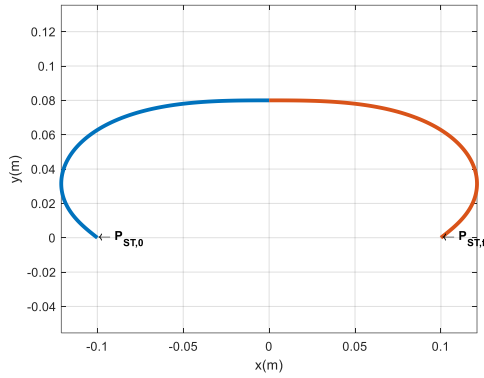


**Fig. 6** The swing phase desired trajectory based on the polynomials function.

The derivative of the polynomial function in Eqs. (17) and (18) with respect to time gives the desired velocity trajectory, which can then be used in the kinematic equations (Equation (15)) to determine the desired joint angles for the robot's leg. Once the desired angles for the two main links are found, the desired angle for the 4-bar mechanism can also be evaluated according to past section. Fig. 7 illustrates the robot's desired joint angles derived from the given trajectory, showing how the robot's leg moves according to the predefined motion path.

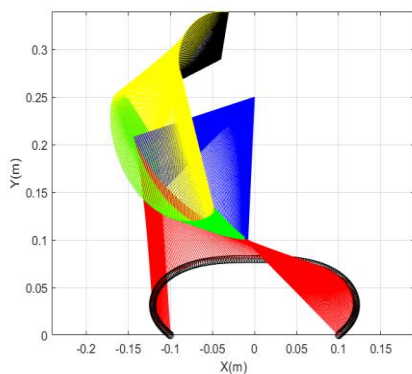


**Fig. 7** The angle of links according to desired trajectory during the motion.

In Fig. 7, the link lengths correspond to the ordinary case presented in Table 1. In the following section, the dynamics of the robot

will be enhanced to simulate the robot's response to the actuator forces.

#### 4-Dynamics equation

Several gaits are inspired by nature, each differing in the number of phases and combinations of leg movements [38]. In this project, the trotting gait has been selected to move the robot. The sequence of leg movements is shown in Table 3. The trotting gait can reach speeds where inertia must be considered in the dynamic equations.

**Table 3:** Leg movement in trotting phase. Each cycle contains two phases.

leg	1	2	1	2	1	2	1	2
Left front		█		█		█		█
Left rear	█		█		█		█	
Right front			█				█	
Right rear		█		█		█		█

To calculate the robot's dynamics, the Lagrange method is applied. Based on the robot's gait, the dynamics are divided into four parts within each cycle. In the first part, two diagonal legs are in the swing phase, while the other two diagonal legs are in the stance phase. Once the swing legs make contact with the ground, the legs switch, and the same pattern is repeated for the other diagonal legs. Thus, each cycle consists of a swing-stance phase for the diagonal legs (four legs) and an impact phase for the swing legs (two legs). The stance phase introduces constraints on the robot's legs, as they can be treated like joints, assuming sufficient friction. Consequently, the Lagrange equation can be expressed as follows [39]:

$$\begin{aligned}
& \underbrace{\left[ \frac{\partial}{\partial \dot{q}} \left( \frac{\partial L}{\partial \dot{q}} \right) \right]}_{[M]} \{\ddot{q}\} \\
& = \{Q\} - \underbrace{\left[ \frac{\partial}{\partial q} \left( \frac{\partial L}{\partial \dot{q}} \right) \right]}_N \{\dot{q}\} + \underbrace{\left\{ \frac{\partial}{\partial t} \left( \frac{\partial L}{\partial \dot{q}} \right) \right\} - \left\{ \frac{\partial L}{\partial q} \right\}}_{\{B\}} \\
& + [a]^T \{\lambda\}
\end{aligned} \tag{19}$$

In Eq. (19),  $L$  represents the Lagrangian, which is the difference between the kinetic energy  $T$  and potential energy  $V$  ( $L = T - V$ ).  $Q$  denotes the virtual forces, while  $q$  and  $\dot{q}$  are the generalized coordinates and velocities, respectively.  $\lambda$  represents the Lagrange multipliers. The matrix  $a$  arises from the constraints and can be written as follows:

$$[a]\{\dot{q}\} + \{b\} = \{0\} \tag{20}$$

To simulate the robot's response, the augmented Lagrange method is used, which can be expressed as follows:

$$\begin{aligned}
& \begin{bmatrix} [M]_{m \times m} & -[a]_{r \times m}^T \\ [a]_{r \times m} & [0]_{r \times r} \end{bmatrix} \begin{Bmatrix} \{\ddot{q}\} \\ \{\lambda\} \end{Bmatrix}_{(m+r) \times 1} \\
& = \begin{Bmatrix} Q - B \\ -\dot{a}\dot{q} - \dot{b} \end{Bmatrix}
\end{aligned} \tag{21}$$

In Eq. (21),  $m$  represents the number of generalized coordinates, while  $r$  denotes the number of constraints.

To verify the correctness of derived equations, the time derivative of the total mechanical energy is examined. In the absence of virtual forces, if the derivative of the total mechanical energy equals zero, it can be concluded that the equations are correct. The time derivative of mechanical energy is expressed as follows:

$$\frac{dE}{dt} = Q^T \dot{q} + \lambda^T a \dot{q} - \frac{\partial L}{\partial t} \tag{22}$$

where  $E$  represents the total mechanical energy, which is the sum of kinetic and potential energy ( $T + V$ ). Due to the high number of constraints in the system, there may be intervals where the constraint equations are not fully satisfied. Therefore, to ensure the validity of the derived equations, the following condition is checked:

$$\frac{dE}{dt} - \lambda^T a \dot{q} = 0 \tag{23}$$

Each leg contains 3 degrees of freedom (DOF), which can be represented by 5 generalized coordinates and 2 constraints. The constraints mentioned here arise from the 4-bar linkage. For example, the right front leg has the generalized coordinates  $\{\theta_1, \theta_2, \theta'_2, \theta'_3, \alpha_1\}$ . Therefore, the robot's legs collectively have a total of 15 generalized coordinates, represented as follows:

$$q_j = \{\theta_{2j-1}, \theta_{2j}, \theta'_{3j-1}, \theta'_{3j}, \alpha_j\}, \quad j = 1, 2, 3, 4 \tag{24}$$

which  $j$  represents the leg number.

If any leg is in the stance phase, additional constraints are applied to it: the velocity of the end effector in the ground plane, due to friction, is equal to zero.

The torso of the robot contains 6 degrees of freedom (DOF) in space, represented as  $\{X, Y, Z, \eta, \psi, \zeta\}$ . The  $\{X, Y, Z\}$  coordinates are expressed in the global coordinate system, while  $\{\eta, \psi, \zeta\}$  represent body-fixed rotations. The first rotation,  $\psi$ , is around the vertical (gravity) axis,  $\zeta$  is around the transverse direction, and the last rotation,  $\eta$ , is around the longitudinal axis. The angular and linear velocity of the main body can be expressed as follows:

$$\vec{V}_{body} = \dot{X}\vec{i} + \dot{Y}\vec{j} + \dot{Z}\vec{k} \quad (25)$$

$$\begin{aligned} \vec{\omega}_{body} &= \dot{\psi}\hat{j}_1 + \dot{\zeta}\hat{k}_2 + \dot{\eta}\hat{i} \\ &= (\dot{\eta} + \dot{\psi} \sin \zeta)\hat{i} \\ &\quad + (\dot{\psi} \cos \zeta \cos \eta \\ &\quad + \dot{\zeta} \sin \eta)\hat{j} + (\dot{\zeta} \cos \eta \\ &\quad - \dot{\psi} \cos \zeta \sin \eta)\hat{k}_2 \end{aligned} \quad (26)$$

In Eqs. (25) and (26), the linear velocity is expressed in the global coordinate system, while the angular velocity is expressed in the body-fixed coordinate system. The calculation of the velocity of the center of gravity of other parts is straightforward and can be related to each other using rotation matrices. During the impact phase, the stance phase changes instantaneously. Due to the short duration of the impact, the configuration of the robot can be assumed to be fixed, but the velocity of its parts can change. To calculate the changes in velocity, the integral of the Lagrange equation is used, as follows:

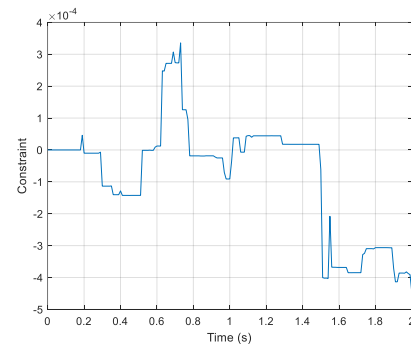
$$\begin{aligned} \begin{bmatrix} [M] & -[a]^T \\ [a] & [0] \end{bmatrix} \begin{Bmatrix} \{\dot{q}\}|_{t=t_1+\Delta t} \\ \{\hat{\lambda}\} \end{Bmatrix} \\ = \begin{Bmatrix} [M]\{\dot{q}\}|_{t=t_1} \\ \{0\} \end{Bmatrix} \end{aligned} \quad (27)$$

Table 4 shows the entire cycle of dynamics and the intervals during which the stance phase constraints are applied.

**Table 4:** The interval for applying the zero-velocity constraint to each leg during simulation is shown in the table. The numbers in the table correspond to the legs, ordered from right front, right rear, left front, to left rear.

Swing & stance				impact				Swing & stance				impact			
1	2	3	4	1	2	3	4	1	2	3	4	1	2	3	4

By simulating the robot's dynamics and verifying the validity of the responses, we can conclude that the dynamic modeling is accurate. Fig. 8 illustrates the satisfaction of constraints, while Fig. 9 depicts the time derivative of the total mechanical energy, taking the constraints into account. These figures confirm the correctness of the modeling. Furthermore, the mean and variance of the total mechanical energy, considering the constraint, are calculated as  $-4.19 \times 10^{-13}$  and  $8.54 \times 10^{-24}$ , respectively. Additionally, when evaluating all constraints together, the mean and variance are  $-8.30 \times 10^{-5}$  and  $7.99 \times 10^{-6}$ , respectively.



**Fig. 8** Average constraint satisfaction in the absence of actuators torques.

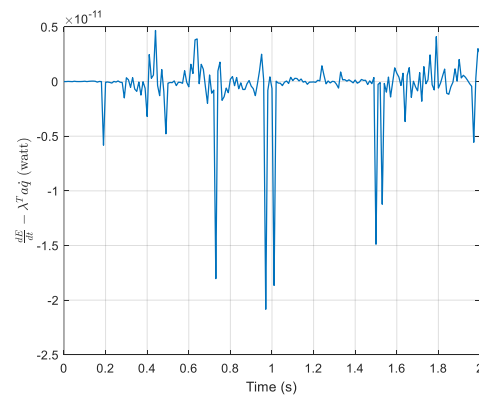


**Fig. 9** Variation of total mechanical energy considering constraints in the absence of actuators torques.

In the following section, the control algorithm for the robot's motion is explained.

## 5- Control algorithm

In each phase of the motion cycle, two legs are in the stance phase while the other two legs are in the swing phase. In the kinematic section, the desired motion and angles for the swing legs are derived. To achieve the desired angles, a PD controller is applied to the actuators. The implemented controller is model-independent, allowing it to be fast enough for real-time applications.

$$u_{\theta_{2i-1}}(t) = K_{p,\theta_{2i-1}}(\theta_{2i-1,desired} - \theta_{2i-1}) + K_{v,\theta_{2i-1}}(\dot{\theta}_{2i-1,desired} - \dot{\theta}_{2i-1}) \quad (28)$$

$$u_{\theta'_{3i}}(t) = K_{p,\theta'_{3i}}(\theta'_{3i,desired} - \theta'_{3i}) + K_{v,\theta'_{3i}}(\dot{\theta}'_{3i,desired} - \dot{\theta}'_{3i}) \quad (29)$$

In Eqs. (28) and (29),  $i$  ranges from 1 to 4, which defines the robot's legs (in each phase, two legs use this control law). The subscript  $i$  indicates the placement of the actuator and its direct effect on the angle.  $K_p$  and  $K_v$  are the proportional and derivative gains, respectively, and the desired variable can be calculated according to the desired motion and inverse kinematics.

The pitch actuator employs a PD controller, with the desired angle during the swing phase consistently set to zero for its direct variables  $\{\alpha_1, \alpha_2, \alpha_3, \alpha_4\}$ .

$$u_{\alpha_i}(t) = K_{p,\alpha_i}(\alpha_{i,desired} - \alpha_i) + K_{v,\alpha_i}(\dot{\alpha}_{i,desired} - \dot{\alpha}_i) \quad (30)$$

The block diagram of the swing phase controller is illustrated in Fig. 10.

The stance phase controller plays a crucial role in the robot's motion. During this phase, the two legs in contact with the ground utilize it to generate the desired forces

necessary for achieving appropriate movement. Zero velocity constraints on the end effector are applied to determine the desired angles that produce these forces. In each phase, there are zero velocity constraints for the stance phase legs (in addition to the constraints imposed by the four-bar mechanism). These constraints can be expressed in the form of  $[a]\{\dot{q}\} = \{0\}$ . By assuming that  $[a]\{\dot{q}\}$  equals vector  $\{r\}$  and employing Jacobian matrices, the desired angles for the stance phase can be calculated. For instance, the equation below defines the desired stance phase angles when the right front and left rear legs are in the stance phase.

$$\begin{Bmatrix} \dot{\theta}_1 \\ \dot{\theta}_2 \\ \dot{\theta}_7 \\ \dot{\theta}_8 \\ \dot{\alpha}_1 \\ \dot{\alpha}_4 \end{Bmatrix} = -[C]^+[D] \begin{Bmatrix} \dot{X} \\ \dot{Y} \\ \dot{Z} \\ \dot{\psi} \\ \dot{\zeta} \end{Bmatrix} \quad (31)$$

The + sign in Eq. (31) denotes the pseudo-inverse operation, which, in the case of square matrices, is equivalent to the inverse function. The matrices  $[C]$  and  $[D]$  are defined as follows:

$$[C] = \begin{bmatrix} \frac{\partial\{r\}}{\partial\theta_1} & \frac{\partial\{r\}}{\partial\theta_2} & \frac{\partial\{r\}}{\partial\theta_7} & \frac{\partial\{r\}}{\partial\theta_8} & \frac{\partial\{r\}}{\partial\alpha_1} & \frac{\partial\{r\}}{\partial\alpha_2} \end{bmatrix} \quad (32)$$

$$[D] = \begin{bmatrix} \frac{\partial\{r\}}{\partial\dot{x}} & \frac{\partial\{r\}}{\partial\dot{y}} & \frac{\partial\{r\}}{\partial\dot{z}} & \frac{\partial\{r\}}{\partial\dot{\psi}} & \frac{\partial\{r\}}{\partial\dot{\zeta}} \end{bmatrix} \quad (33)$$

In Eq. (31),  $\dot{\eta}$  is set to zero to assume that the robot remains stable during movement. In practical applications, the angle  $\eta$  is maintained at a constant value by selecting an appropriate desired movement in the plane. Several criteria, such as the Zero Moment Point (ZMP) and the Foot Rotation Indicator (FRI), can be utilized for this purpose [40]. After determining the desired angle from the equation above, a PD controller will be applied to the two pitch

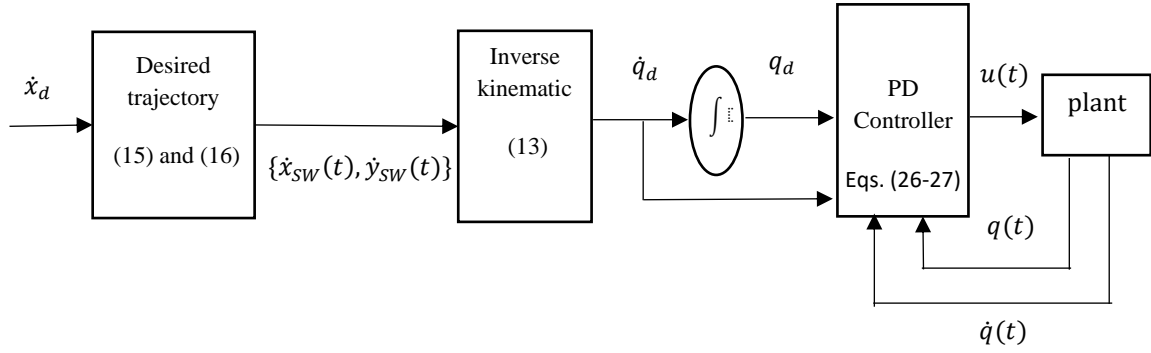


Fig. 10 Block diagram of swing phase controller for pitching.

angles of the robot, as described in the following equation.

$$u_{\theta_{2i-1}}(t) = K_{p,\theta_{2i-1}}(\theta_{2i-1,desired} - \theta_{2i-1}) + K_{v,\theta_{2i-1}}(\dot{\theta}_{2i-1,desired} - \dot{\theta}_{2i-1}) \quad (34)$$

$$u_{\theta_{2i}}(t) = K_{p,\theta_{2i}}(\theta_{2i,desired} - \theta_{2i}) + K_{v,\theta_{2i}}(\dot{\theta}_{2i,desired} - \dot{\theta}_{2i}) \quad (35)$$

In comparison to the swing phase, the structure of the controller remains the same; however, the desired angles are derived from Eq. (31) instead of Eq. (15). Additionally, to maintain the height of the torso, an outer-loop proportional (P)

controller has been incorporated. This addition addresses the issue of the robot potentially moving downward during forward stepping due to numerical errors.

$$\dot{y}_{desired} = K_y(y_{desired} - y(t)) \quad (36)$$

The control loop diagram is shown in Fig. 11.

## 6- Results

In this section, two cases of trajectory control have been investigated. In the first case, the robot's heading is maintained constant while it moves in both the transverse and longitudinal directions.

Fig. 12 displays the X, Y, and Z coordinates relative to time for a desired velocity of

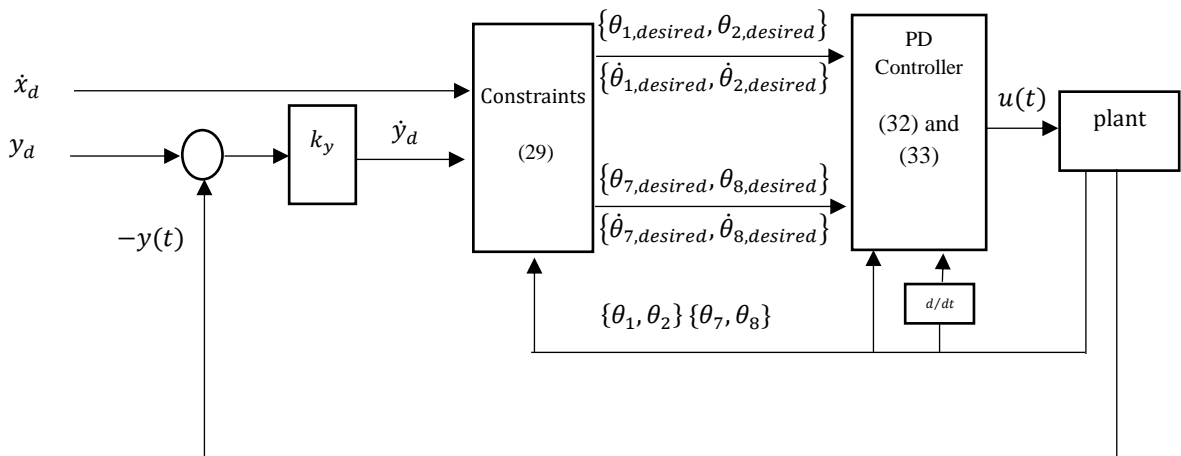
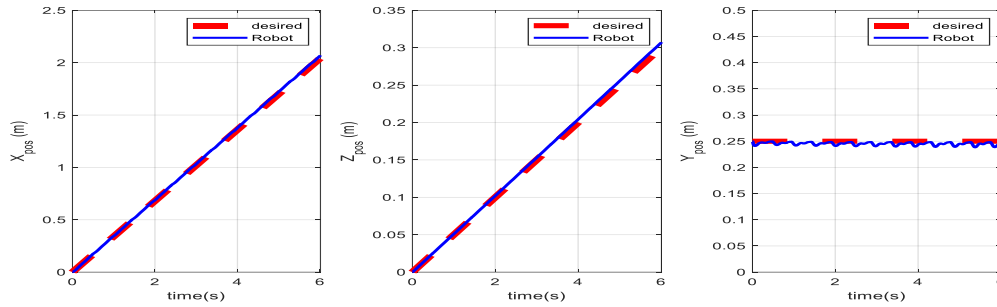


Fig. 11 Block diagram of stance phase controller.

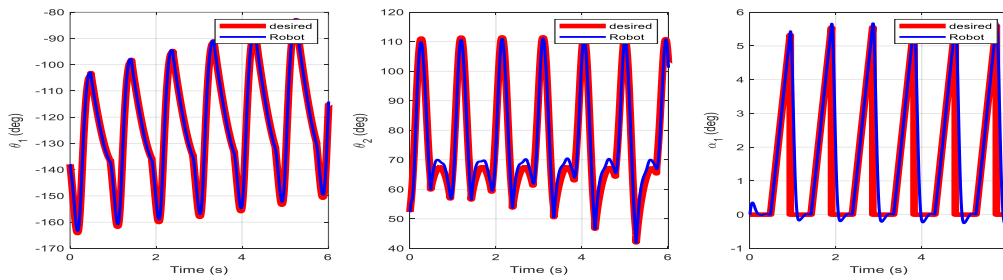
$\dot{X} = 0.32m/s$  and  $\dot{Z} = 0.05m/s$ . It is evident that the robot successfully tracks the desired trajectory throughout the motion. Fig. 13 illustrates the desired and simulated angles of the robot's links for the right front leg. The desired angles are derived from two

distinct sets of rules, which correspond to the stance and swing phases.

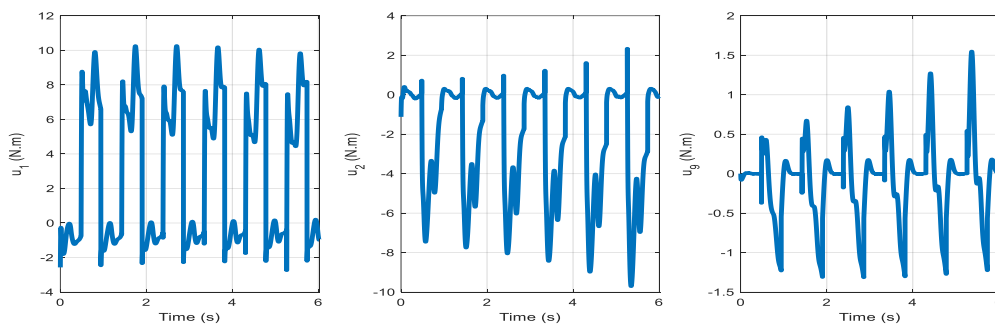
The actuator inputs, as illustrated in Fig. 14 are specifically shown for the right front leg.



**Fig. 12** Linear coordinates of torso relative to time in case of constant heading scenario.

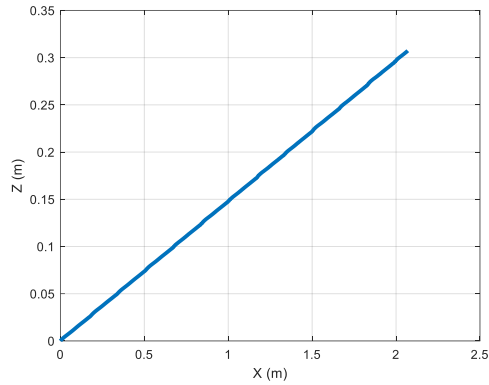


**Fig. 13** Desired and simulated angle in case of constant heading for right front leg.



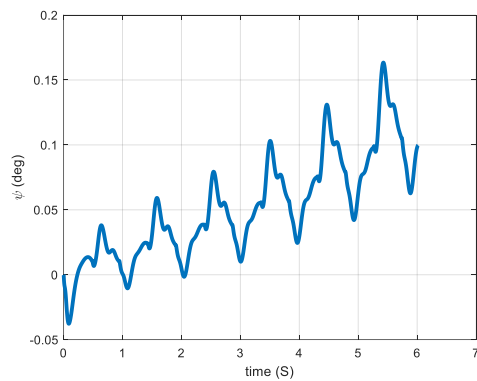
**Fig. 14** Control output of right front leg in case of constant heading.

Fig. 15 illustrates the robot's position in the plane.



**Fig. 15** Planar movement of robot in case of constant heading.

In the aforementioned scenario, the robot's heading is maintained at a constant angle. Fig. 16 illustrates the variation of the heading angle throughout the motion.



**Fig. 16** Heading of the robot during constant heading scenario.

In the second scenario, the robot's heading angle is varied to facilitate movement within the plane. By adjusting the heading, the robot's desired transverse coordinate changes, as described by the following equation:

$$\dot{Z} = -\dot{X} \tan \psi \quad (37)$$

Fig. 17 illustrates the robot's movement within the plane, maintaining a desired coordinate of  $\dot{X} = 0.32m/s$  with a heading rate of  $\dot{\psi} = -7deg/s$  until 4.4 seconds, after which the heading rate changes to  $\dot{\psi} = 7deg/s$  for the remainder of the simulation.

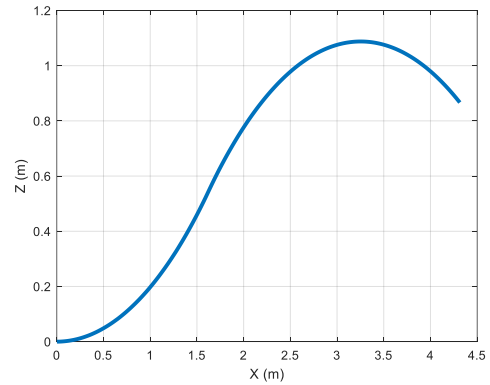


**Fig. 17** Planar movement of robot in case of variable heading.

Fig. 18 depicts the corresponding variation of the robot's heading angle.

The torso coordinates of the robot as a function of time are presented in Fig. 19. Moreover, Fig. 20 illustrates the desired and actual angles of the robot's front right leg, while Fig. 21 presents the corresponding controller output.

Fig. 22 illustrates the frames of the robot's movement with a variable heading.

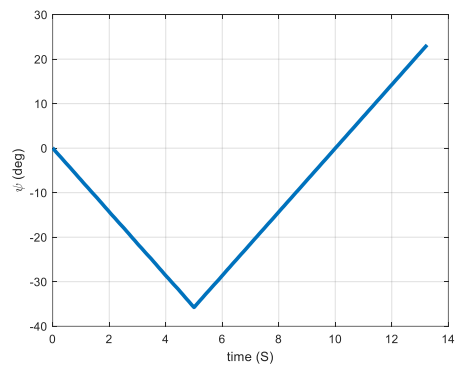


**Fig. 18** Heading angle of robot in case of variable heading control.

To plan a desired trajectory that the robot can follow, the concept of the Zero Moment Point (ZMP) is employed. According to this principle, the robot's stability is maintained ( $\dot{\eta} = 0$ ) as long as the ZMP lies within the boundary defined by the line connecting the contact points. Generally, the ZMP is the point at which the resultant planar moment

due to the reaction forces is zero. Considering the dynamics of the robot, this point can be calculated using the following equations:

$$\begin{cases} z_{zmp} = \frac{\dot{H}_{O,X} + Y_{zmp}\dot{P}_Y + z_{C.G}mg}{\dot{P}_Y + mg} \\ x_{zmp} = \frac{-\dot{H}_{O,Z} - Y_{zmp}\dot{P}_X + x_{C.G}mg}{\dot{P}_Y + mg} \end{cases} \quad (38)$$

where  $H$  is angular momentum and  $P$  is linear momentum of robot.

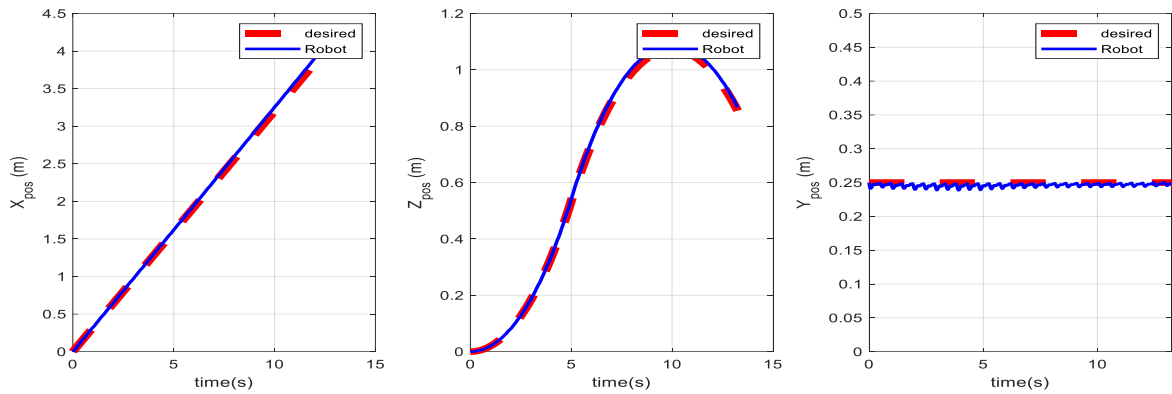


Fig. 19 Linear coordinates of torso relative to time in case of variable heading.

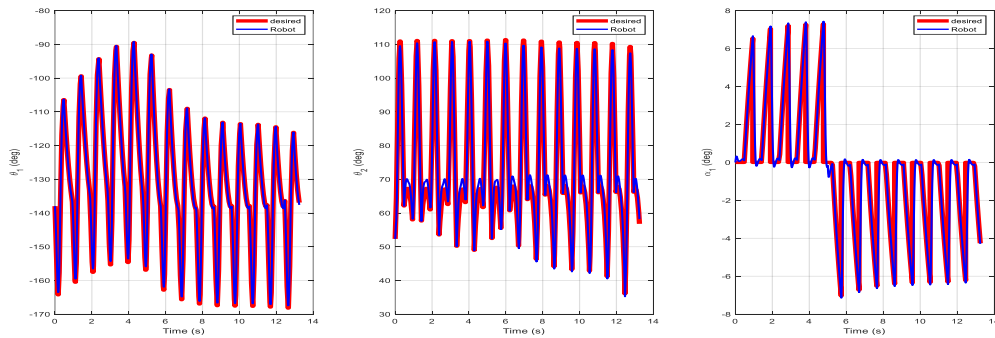


Fig. 20 Desired and simulated angle of right front leg in case of variable heading.

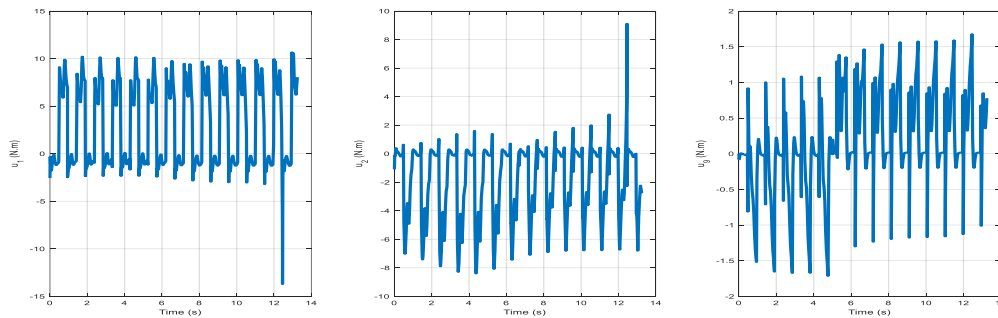
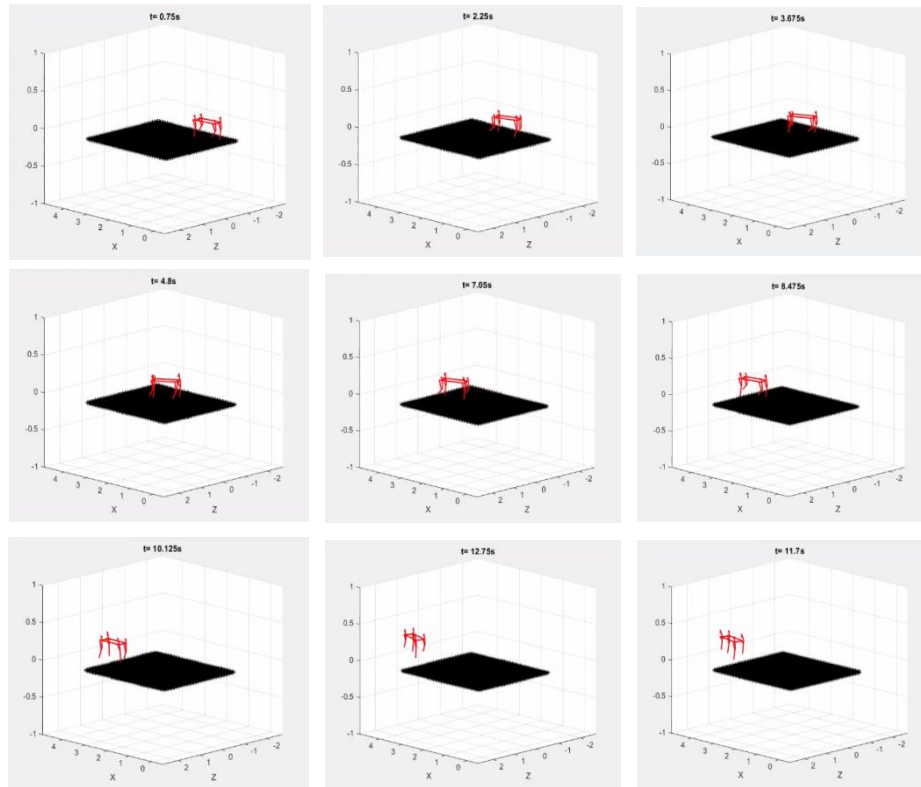


Fig. 21 Actuator input for right front leg in case of variable heading.

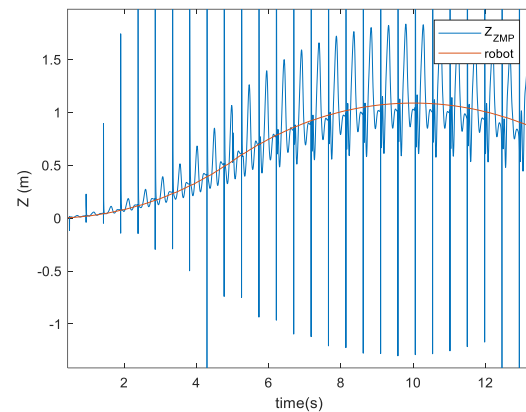


**Fig. 22** Movement frame of robot in case of variable heading.

By calculating the Zero Moment Point (ZMP) in relation to the center of gravity (CoG), a desired trajectory can be formulated that ensures dynamic stability. Fig. 23 illustrates the ZMP alongside the CoG in scenarios involving variable heading.

The high frequency variations observed in Fig. 23 are attributed to the robot's impact, where the Zero Moment Point (ZMP) criteria apply. These brief intervals are considered negligible.

The results presented thus far have been simulated based on the standard responses outlined in Table 1. To illustrate the impact of optimization on actuator torques, two simulations were conducted for the robot's forward movement, utilizing identical proportional and derivative gains. The sole variation lies in the lengths of the four-bar mechanism, as specified in Table 1.



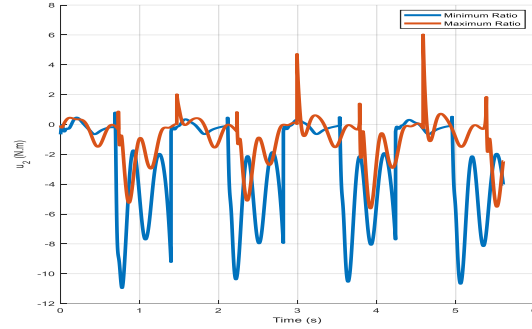
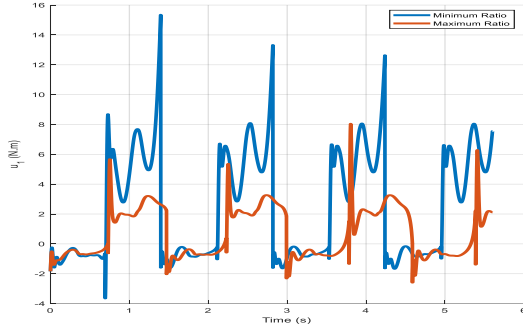
**Fig. 23** Zero moment point and center of gravity (which lies within the supporting line) comparison.

Fig. 24 compares the actuator torque of the right front rolling actuator for two different link configurations: one representing the maximum ratio from the table and the other the minimum ratio.

As illustrated in Fig. 24, the optimization algorithm enables the robot to require less force, particularly during the stance phase, due to the higher transmission ratio. The

root mean squared (RMS) values for the two actuators with the maximum ratio are 1.8454 and 1.76, whereas the corresponding values for the minimum ratio are 4.3543 and

4.1043. This clearly demonstrates the greater efficiency achieved with the lengths corresponding to the maximum ratio.



**Fig. 24** Actuator torques comparison for two different links length according to Table 1:

To validate Eq. (8), the four-bar mechanism has been excluded, and the knee actuator torque is transformed to the knee joint as described by Eq. (8). In the equation below, the dynamic term is neglected, assuming the robot operates in a semi-static manner. Under this assumption, the only influential factors are the input torques and ground forces.

$$\begin{aligned}
 u_{\theta_{2i-1}} - \lambda_y \{ l_h \cos \theta_{2i-1} + l_e \cos(\theta_{2i-1} + \theta_{2i}) \} \\
 - \lambda_x \{ l_h \sin \theta_{2i-1} \\
 + l_e \sin(\theta_{2i-1} + \theta_{2i}) \} \\
 \approx \frac{l_1 \sin a}{l_3 \sin b} u_{\theta_{3i}}
 \end{aligned}
 \tag{39}$$

The terms  $u_{\theta_{2i-1}}$  and  $u_{\theta_{3i}}$  represent the actuator torques, where  $i$  denotes the robot's leg. This equation is valid only for legs in contact with the ground. The ground forces,  $\lambda_x$  and  $\lambda_y$ , are calculated during the robot's simulation. Fig. 25 demonstrates the accuracy of Eq. (39), verifying that Eq. (8) effectively captures the transformed torque. This result confirms that the robot moves in a semi-static manner during the stance phase.

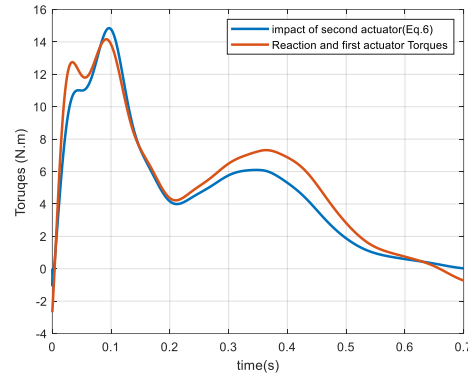


**Fig. 25** Semi-static manner of robot leg in stance phase and the impact of transferring knee torque.

The PD gains used throughout the article are selected based on empirical tuning, and their corresponding values are provided in Table 5.

**7- Conclusion**

In this study, a PD controller based on the robot's kinematics has been proposed for a quadruped robot. To reduce leg inertia, all actuators are positioned near the hip joint, and an optimized four-bar mechanism is employed to transmit torque to the knee joint.

**Table 5:** PD selected values in the simulation.

Phase	gain	value
Swing Phase	$K_{p,\theta_{2i-1}}$ (Equation (28))	40
	$K_{v,\theta_{2i-1}}$ (Equation (28))	0.9
	$K_{p,\theta_{3i}}$ (Equation (29))	8
	$K_{v,\theta_{3i}}$ (Equation (29))	0.2
	$K_{p,\alpha_i}$ (Equation (30))	5
	$K_{v,\alpha_i}$ (Equation (30))	0.4
Stance Phase	$K_{p,\theta_{2i-1}}$ (Equation (34))	640
	$K_{v,\theta_{2i-1}}$ (Equation (34))	8
	$K_{p,\theta_{2i}}$ (Equation (35))	110
	$K_{v,\theta_{2i-1}}$ (Equation (35))	3
	$K_y$ (Equation (36))	1.2
	$K_{p,\alpha_i}$ (Equation (30))	700
	$K_{v,\alpha_i}$ (Equation (30))	50

The optimization's effectiveness is demonstrated throughout the paper by minimizing and maximizing the objective function. Additionally, the robot's kinematic and dynamic equations are derived to simulate its response in various scenarios, including fixed and variable heading. The controller is designed for real-time implementation, and the optimization enhances the reaction forces while overall reducing the robot's weight. For future work, it is recommended to explore multi-objective algorithms to optimize the robot's link lengths during both the swing and stance phases simultaneously. Moreover, real-time trajectory planning could be integrated to maintain stability in the presence of uncertainties.

## References

- [1] Biswal, P., & Mohanty, P. K. (2021). Development of quadruped walking robots: A review. *Ain Shams Engineering Journal*, 12 (2), 2017–2031. <https://doi.org/https://doi.org/10.1016/j.asej.2020.11.005>
- [2] Chen, J.-P., San, H.-J., Wu, X., & Xiong, B.-Z. (2022). Structural design and gait research of a new bionic quadruped robot. *Proceedings of the Institution of Mechanical Engineers, Part B: Journal of Engineering Manufacture*, 236 (14), 1912–1922. <https://doi.org/10.1177/0954405421995663>
- [3] Zhou, Q., Yang, S., Jiang, X., Zhang, D., Chi, W., Chen, K., Zhang, S., Li, J., Zhang, J., Wang, R., Li, J., Zhang, Y., Wang, H., Wang, S., Xiang, L., Zheng, Y., & Zhang, Z. (2024). Max: A wheeled-legged quadruped robot for multimodal agile locomotion. *IEEE Transactions on Automation Science and Engineering*, 21 (4), 7562–7582. <https://doi.org/10.1109/TASE.2023.3345876>
- [4] Hutter, M., Gehring, C., Jud, D., Lauber, A., Bellicoso, C. D., Tsounis, V., Hwangbo, J., Bodie, K., Fankhauser, P., Bloesch, M., Diethelm, R., Bachmann, S., Melzer, A., & Hoepflinger, M. (2016). Anymal - a highly mobile and dynamic quadrupedal robot. 2016 IEEE/RSJ International Conference on Intelligent Robots and Systems (IROS), 38–44. <https://doi.org/10.1109/IROS.2016.7758092>
- [5] Abrar, M. M., & Islam, R. (2020). Design and development of a biologically inspired robotic cat for research and education. 2020 30th International Conference on Computer Theory and Applications (ICCTA), 82–87. <https://doi.org/10.1109/ICCTA52020.2020.9477678>
- [6] Sun, Y., Pancheri, F., Rehekampff, C., & Lueth, T. C. (2024). Turbot: A turtleinspired quadruped robot using topology optimized soft-rigid hybrid legs. *IEEE/ASME Transactions on Mechatronics*, 29 (4), 3193–3202. <https://doi.org/10.1109/TMECH.2024.3404667>
- [7] Seok, S., Wang, A., Chuah, M. Y., Hyun, D. J., Lee, J., Otten, D. M., Lang, J. H., & Kim, S. (2015). Design principles for energy-efficient legged locomotion and implementation on the mit cheetah robot. *IEEE/ASME Transactions on Mechatronics*, 20 (3), 1117–1129.

- <https://doi.org/10.1109/TMECH.2014.2339013>
- [8] Taheri, H., & Mozayani, N. (2023). A study on quadruped mobile robots. *Mechanism and Machine Theory*, 190, 105448. <https://doi.org/https://doi.org/10.1016/j.mechmachtheory.2023.105448>
- [9] Raibert, M., Blankespoor, K., Nelson, G., & Playter, R. (2008). Bigdog, the rough-terrain quadruped robot [17th IFAC World Congress]. *IFAC Proceedings Volumes*, 41 (2), 10822–10825. <https://doi.org/https://doi.org/10.3182/20080706-5-KR-1001.01833>
- [10] Zhaoxi, L. (2022). A review of motion control methods and bionic control theory for quadruped robots. *2022 IEEE Conference on Telecommunications, Optics and Computer Science (TOCS)*, 928–931. <https://doi.org/10.1109/TOCS56154.2022.10016139>
- [11] <https://www.facebook.com/48576411181>. (n.d.). Whoa: Boston Dynamics Announces New WildCat Quadruped Robot — [spectrum.ieee.org](https://spectrum.ieee.org) [[Accessed 09-09-2024]].
- [12] Chignoli, M., & Wensing, P. M. (2020). Variational-based optimal control of underactuated balancing for dynamic quadrupeds. *IEEE Access*, 8, 49785–49797. <https://doi.org/10.1109/ACCESS.2020.2980446>
- [13] Hattori, A. (2020, May). Design of a high torque density modular actuator for dynamic robots [Master's thesis]. Massachusetts Institute of Technology, Department of Mechanical Engineering.
- [14] Wait, K. W., & Goldfarb, M. (2014). A pneumatically actuated quadrupedal walking robot. *IEEE/ASME Transactions on Mechatronics*, 19 (1), 339–347. <https://doi.org/10.1109/TMECH.2012.2235078>
- [15] Majithia, A., Shah, D., Dave, J., Kumar, A., Rathee, S., Dogra, N., H. M, V., Chiniwar, D., & Hiremath, S. (2024). Design, motions, capabilities, and applications of quadruped robots: A comprehensive review [Publisher Copyright: Copyright © 2024 Majithia, Shah, Dave, Kumar, Rathee, Dogra, H. M., Chiniwar and Hiremath.]. *Frontiers in Mechanical Engineering*, 10. <https://doi.org/10.3389/fmech.2024.1448681>
- [16] Tedeschi, F., & Carbone, G. (2014). Design issues for hexapod walking robots. *Robotics*, 3 (2), 181–206. <https://doi.org/10.3390/robotics3020181>
- [17] Tsitsimpelis, I., Taylor, C. J., Lennox, B., & Joyce, M. J. (2019). A review of ground-based robotic systems for the characterization of nuclear environments. *Progress in Nuclear Energy*, 111, 109–124. <https://doi.org/https://doi.org/10.1016/j.pnucene.2018.10.023>
- [18] Wang, H., Fang, D., Sang, L., Wang, Y. J., Wen, Y., & Chen, N. (2013). Gait planning of the quadruped walking chair robot with parallel leg mechanism. *2013 IEEE International Conference on Mechatronics and Automation*, 13–18. <https://api.semanticscholar.org/CorpusID:18019>
- [19] Hongjun, M., Shupeng, Z., Wei, Z., & Yuke, R. (2024). Design and control of a new pneumatic quadruped soft robot based on honeycomb structure. *IEEE Access*, PP, 1–1. <https://doi.org/10.1109/ACCESS.2024.3427844>
- [20] Lee, J., Coutinho, A., Oh, N., Jang, J. H., Park, Y. J., Namgung, H., Oh, D. G., & Rodrigue, H. (2024). Vacuum-driven class-2 tensegrity-based mechanism for quadrupedal robot motion. *IEEE Robotics and Automation Letters*, 9 (7), 6520–6527. <https://doi.org/10.1109/LRA.2024.3407410>
- [21] Yang, J.-M. (2008). Two-phase discontinuous gaits for quadruped walking machines with a failed leg. *Robotics and Autonomous Systems*, 56 (9), 728–737. <https://doi.org/https://doi.org/10.1016/j.robot.2008.01.002>
- [22] Ju, Z., Wei, K., Jin, L., & Xu, Y. (2024). Investigating stability outcomes across diverse gait patterns in quadruped robots: A comparative analysis. *IEEE Robotics and Automation Letters*, 9 (1), 795–802. <https://doi.org/10.1109/LRA.2023.3338064>
- [23] Khoramshahi, M., Spröowitz, A., Tuleu, A., Ahmadabadi, M. N., & Ijspeert, A. J. (2013). Benefits of an active spine supported bounding locomotion with a small compliant quadruped robot. *2013 IEEE International Conference on Robotics and Automation*, 3329–3334. <https://doi.org/10.1109/ICRA.2013.6631041>

- [24] Wang, C., Fan, C., Yang, Y., Zhan, M., Shao, H., & Ma, B. (2020). Realization of a bio-inspired cheetah robot with a flexible spine. 2020 IEEE International Conference on Mechatronics and Automation (ICMA), 1185–1190. <https://doi.org/10.1109/ICMA49215.2020.9233690>
- [25] Liu, H., & Yuan, Q. (2024). Safe and robust motion planning for autonomous navigation of quadruped robots in cluttered environments. IEEE Access, 12, 69728–69737. <https://doi.org/10.1109/ACCESS.2024.3401827>
- [26] Fan, Y., Pei, Z., Wang, C., Li, M., Tang, Z., & Liu, Q. (2024). A review of quadruped robots: Structure, control, and autonomous motion. Advanced Intelligent Systems, 6 (6), 2300783. <https://doi.org/10.1002/aisy.202300783>
- [27] Hu, C., Mei, T., Sun, S., Liu, Y., Wu, X., & Zhang, Y. (2013). Cpg-based control system for foot locomotion of gecko-inspired robot. 2013 Fifth International Conference on Measuring Technology and Mechatronics Automation, 409–414. <https://doi.org/10.1109/ICMTMA.2013.103>
- [28] Wasista, S., Tjandrasa, H., & Wibisono, W. (2020). Quadruped robot control base on adaptive neuro-fuzzy inference system with v-rep simulator. 2020 3rd International Conference on Information and Communications Technology (ICOIACT), 280–285. <https://doi.org/10.1109/ICOIACT50329.2020.9332008>
- [29] Yu, H., Gao, H., & Deng, Z. (2021). Toward a unified approximate analytical representation for spatially running spring-loaded inverted pendulum model. IEEE Transactions on Robotics, 37 (2), 691–698. <https://doi.org/10.1109/TRO.2020.2976304>
- [30] Zhang, Z., Chang, X., Ma, H., An, H., & Lang, L. (2023). Model predictive control of quadruped robot based on reinforcement learning. Applied Sciences, 13 (1). <https://doi.org/10.3390/app13010154>
- [31] Di Carlo, J., Wensing, P. M., Katz, B., Bledt, G., & Kim, S. (2018). Dynamic locomotion in the mit cheetah 3 through convex model-predictive control. 2018 IEEE/RSJ International Conference on Intelligent Robots and Systems (IROS), 1–9. <https://doi.org/10.1109/IROS.2018.8594448>
- [32] Kim, D., Lee, J., Ahn, J., Campbell, O., Hwang, H., & Sentis, L. (2018). Computationally-robust and efficient prioritized whole-body controller with contact constraints. 2018 IEEE/RSJ International Conference on Intelligent Robots and Systems (IROS), 1–8. <https://doi.org/10.1109/IROS.2018.8593767>
- [33] Xing, B., Liu, Y., Zhirui, W., Liang, Z., Zhao, J., Su, B., & Jiang, L. (2021). Design of the anti-disturbance virtual model controller for quadruped robot, 4359–4365. <https://doi.org/10.1109/CCDC52312.2021.9602160>
- [34] Tanikawa, T., Masuda, Y., & Ishikawa, M. (2021). A reciprocal excitatory reflex between extensors reproduces the prolongation of stance phase in walking cats: Analysis on a robotic platform. Frontiers in Neurorobotics, 15. <https://doi.org/10.3389/fnbot.2021.636864>
- [35] McKenzie, J. E. (2012). Design of robotic quadruped legs [Master's thesis]. Massachusetts Institute of Technology, Department of Mechanical Engineering.
- [36] Freudenstein, F. (July 1, 2022). "An Analytical Approach to the Design of Four-Link Mechanisms." ASME. Trans. ASME. April 1954; 76(3): 483–489.
- [37] Zeng, X., Zhang, S., Zhang, H., Li, X., Zhou, H., & Fu, Y. (2019). Leg trajectory planning for quadruped robots with high-speed trot gait. Applied Sciences, 9 (7). <https://doi.org/10.3390/app9071508>
- [38] Hildebrand, M. (1989). The Quadrupedal Gaits of Vertebrates: The timing of leg movements relates to balance, body shape, agility, speed, and energy expenditure. BioScience, 39 (11), 766–775. <https://doi.org/10.2307/1311182>
- [39] Ginsberg, J. H. (1995). Further Concepts in Analytical Mechanics. In Advanced Engineering Dynamics (pp. 309–388). chapter, Cambridge: Cambridge University Press.
- [40] Popovic, M. B., Goswami, A., & Herr, H. (2005). Ground reference points in legged locomotion: Definitions, biological trajectories and control implications. The International Journal of Robotics Research, 24 (12), 1013–1032. <https://doi.org/10.1177/0278364905058363>